Superionic conducting halide frameworks enabled by interface-bonded halides

Jiamin Fu[1,2†], Shuo Wang[3†], Jianwen Liang[1†] Sandamini H Alahakoon[2], Duojie Wu[4], Jing Luo[1], Hui Duan[1], Shumin Zhang[1,2], Feipeng Zhao[1], Weihan Li[1], Minsi Li[1], Xiaoge Hao[1], Xiaona Li[1], Jiatang Chen[5], Ning Chen[6], Graham King[6], Lo-Yueh Chang[7], Ruying Li[1], Yining Huang[2], Meng Gu[4], Tsun-Kong Sham[2*], Yifei Mo[3*], Xueliang Sun[1*]

[1] Department of Mechanical and Materials Engineering, University of Western Ontario, London, Ontario, N6A 5B9, Canada

[2] Department of Chemistry, University of Western Ontario, London, Ontario, N6A 5B7, Canada

[3] Department of Materials Science and Engineering, University of Maryland, College Park, MD 20742, USA.

[4] Department of Materials Science and Engineering, Southern University of Science and Technology, Shenzhen 518055, China

[5] Chemical Engineering, McMaster University, Hamilton, ON, L8S 4M1, Canada

[6] Canadian Light Source Inc., University of Saskatchewan, Saskatoon, Saskatchewan, S7N 2V3, Canada

[7] National Synchrotron Radiation Research Centre, 101 Hsin-Ann Road, Hsinchu, 30076, Taiwan

[†] These authors contributed equally to this work

* Corresponding authors: tsham@uwo.ca; yfmo@umd.edu; xsun9@uwo.ca

Abstract:

The revival of ternary halides Li-M-X (M = Y, In, Zr, etc.; X = F, Cl, Br) as solid-state electrolytes (SSEs) shows promise in realizing practical solid-state batteries due to their direct compatibility toward high-voltage cathodes and favorable room-temperature ionic conductivity. Most of the reported superionic halide SSEs have a structural pattern of $[MCl_6]^{x-}$ octahedra and generate a tetrahedron-assisted Li-ion diffusion pathway. Here, we report a new class of zeolite-like halide frameworks, $SmCl_3$ for example, in which 1-dimensional channels are enclosed by $[SmCl_9]^{6-}$ tricapped trigonal prisms to provide a short jumping distance of 2.08 Å between two octahedrons for Li-ion hopping. The fast Li-ion diffusion along the channels was verified through *ab initio* molecular dynamics simulations. Similar to zeolites, the $SmCl_3$ framework can graft halide species onto it to obtain mobile ions without altering the base structure, achieving an ionic conductivity over 10^{-4} S cm^{-1} at 30 °C with LiCl as the adsorbent. Moreover, the universality of the interface-bonding behavior and ionic diffusion in a class of frameworks was demonstrated, presenting ionic conductivities ranging from 10^{-6}-10^{-3} S/cm. It is suggested that the ionic conductivity of the $LnCl_3$/halide composite (Ln = La-Gd) is likely in correlation with the ionic conductivity of halide, interfacial bonding, and framework composition/dimensions. This work reveals a potential class of halide structures for superionic conductors and opens up a new frontier for constructing zeolite-like frameworks in halide-base materials, which will promote the innovation of superionic conductor design and contribute to a broader selection of halide SSEs.

Keywords: halide electrolytes, solid-state electrolyte, all-solid-state Li-ion batteries, framework materials, zeolites, ionic diffusion

Introduction

The booming market of electric vehicles today hinges on state-of-the-art energy storage technologies, especially, their durability and safety are priorities.[1] All-solid-state Li-ion batteries (ASSLIBs) are a potential candidate due to their high energy density and instinct safety derived from low flammability,[2] but the gap between laboratory demonstration and industrial applications remains large.[3] Recently, the revival of ternary halides with Li-M-Cl (M = Y, Er, In, Zr, etc.) as solid-state electrolytes (SSEs) shows promise in closing the gap due to their favorable room-temperature ionic conductivity and compatibility toward high-voltage cathodes.[4-10] A wide range of halide synthesis routes, including water-mediated synthesis[5] and ammonia-assisted synthesis[11], is available to meet different production needs. Among the increasingly reported Li-M-Cl SSEs since the first report of Li_3YCl_6 by Tetsuya Asano et al.[4], such as Li_3InCl_6,[5] Li_2ZrCl_6,[12-13] Li_xScCl_{3+x},[6, 10] Li_3ErCl_6,[14] etc.,[15-16] they all share a similar structural pattern. The ionic radii of the metal atoms in Li-M-Cl are close, such as Li^+ (76 pm), In^{3+} (80 pm), Sc^{3+} (74.5 pm), Zr^{4+} (72 pm), and Y^{3+} (90 pm) according to the Shannon-Prewitt effective ionic radius.[17] Within this range of ionic radii, metal halides form $[MCl_6]^{x-}$ octahedra with anionic CCP (cubic closest packed) or HCP (hexagonal closest packed) stacks, generating a tetrahedron-assisted lithium-ion diffusion pathway (such as octahedron-tetrahedron-octahedron).[18-20] Beyond these, a few halides with other metallic elements have been reported to have high ionic conductivity so far. We believe that there are potential ion-conducting structures that might have been overlooked.

If the ionic radius of the immobile metal elements in the chloride electrolytes further increases, the metal-halide polyhedra in the structure will transition from six-fold coordination to eight- or nine-fold coordination. There is an interesting group of rare-earth halides MCl_3 (M = La-Sm) with nine-fold coordination as shown in **Figure 1(a)**, in which MCl_3 forms a *P6₃/m* lattice with 1-dimensional(1D) channels of vacancies along the *c*-axis. It is worth noting that these abundant channels have a similar pore size to that of zeolites, potentially forming a framework for ion diffusion. Other framework materials such as metal-organic frameworks (MOFs) and zeolites have shown great promise for the fabrication of high-performance SSEs through introducing free Li^+, Na^+, or Mg^{2+} ions,[21-25] presenting decent ionic conductivities. Benefiting from the rich porosity, controllable functionality, and modularity, framework materials provide an ideal platform for designing fast ionic conductors. Dated back to 1994, $Na_{3x}M_{2-x}Cl_6$ (M = La-Sm, *P6₃/m*) was reported by Lissner et al.[26], where Na-ions partially occupy the M site, and the rest of the Na-ions are located in the channel vacancy sites. These abundant connected octahedral voids provide a short ion jumping distance, accommodating fast sodium diffusion.[27] However, the Na-ion conductivity reported by Lissner et al.[27] was still well below the requirement for practical application (> 10^{-4} S/cm). As for Li-ion diffusion, to the best of our knowledge, no

stable Li analogs of $Li_{3x}M_{2-x}Cl_6$ have been reported so far due to the large mismatch between the ionic radii of Li^+ (76 pm) and M^{3+} in MCl_3 (M = La-Sm, 122 pm -113 pm). The possibility of Li-ion diffusion in halide-based framework materials has not been addressed. We believe that Li-ions could be highly mobile in the channels of the halide frameworks without altering the framework structure, potentially achieving high Li-ion conductivity.

In this work, the Li-ion diffusion in the $SmCl_3$ framework was studied for the first time through a combination of theoretical calculations and experiments. The $SmCl_3$ lattice with topologies akin to inorganic zeolites was presented in **Figure 1 (b-c)**, where the 1D hexagonal channels along the *c* axis with an inner diameter of ~ 4.53 Å are comparable with the typical zeolite ZSM-5 with a nanopore size of ~ 5.4 Å. The *ab initio* molecular dynamics (AIMD) simulations confirmed the fast Li-ion diffusion in the 1D channels. Experimentally, the ball-milling synthesized $SmCl_3 \cdot 0.5LiCl$ composite (BM-$SmCl_3 \cdot 0.5LiCl$) exhibited a drastic difference in Li-ion conductivity (~1×10^{-4} S/cm) compared to co-melting synthesized composite (CM-$SmCl_3 \cdot 0.5LiCl$) and ball-milled LiCl (BM-LiCl) (both ~ 10^{-8} S/cm) at room temperature (RT). The long-range and short-range structures of the ball-milled samples were systematically studied by X-ray diffraction (XRD), pair distributed function (PDF), and extended X-ray absorption fine structure (EXAFS). Results suggested that the $SmCl_3$ cluster with LiCl grafted around is responsible for the high conductivity. The mechanism was further confirmed through an electronic structure study via X-ray photoelectron spectroscopy (XPS) and X-ray absorption spectroscopy (XAS). The relationship between ionic diffusion behaviors and the bound state of the $SmCl_3$ framework was studied by *in-situ* XRD and nuclear magnetic resonance (NMR) analyses. Moreover, the universality of the interfacial bonding behavior and ionic diffusion of the class of framework was demonstrated, presenting ionic conductivities ranging from 10^{-6}-10^{-3} S/cm. All-solid-state batteries using an $SmCl_3$ framework-based SSE demonstrated excellent electrochemical performances at room temperature. This work reveals a new promising class of halide structures for fast Li-ion conductors. The systematic study of the formation and ion diffusion mechanisms shall broaden the horizon of superionic conductor design and contribute to a wider selection of SSEs.

Results and discussion

The $SmCl_3$ has a UCl_3-type structure ($P6_3/m$) with the Cl and Sm atoms occupying 6h and 2c Wyckoff sites, respectively. The Sm is coordinated by nine Cl to form tricapped trigonal prisms of $[SmCl_9]^{6-}$. The edge-sharing $[SmCl_9]^{6-}$ polyhedra enclose 1D channels of octahedral voids along the *c*-axis direction. The $SmCl_3$ lattice with topologies akin to inorganic zeolites was presented in **Figure 1(b, c)**. The 1D hexagonal channels along the *c* axis are clearly shown in **Figure 2(a)** with an inner diameter of ~ 4.52 Å and a short distance of ~ 2.08 Å between two adjacent cation vacancies. To investigate the ionic diffusion in the 1D channels, we performed AIMD simulations on the model system of $Li_{0.17}SmCl_3$ by incorporating Li into the vacant sites of $SmCl_3$ (see Methods for details). The AIMD simulations reveal fast Li^+ diffusion in the 1D diffusion channels, as shown in the probability density of Li-ion during AIMD simulation **(Figure 2(b))**. The Li ions migrate between equivalent distorted octahedral sites through a shared triangle bottleneck as observed in the trajectories of AIMD simulations, showing a low diffusion barrier of 0.11 ± 0.01 eV in the Arrhenius plot **(Figure 2(c))**.

Given such a fast ionic diffusion in theoretical study, we have conducted both co-melting (CM) and ball-milling (BM) methods to synthesize a Li-containing $SmCl_3$ framework; LiCl was chosen to provide Li-ions for the $SmCl_3$ framework, and products are hence for the denoted CM-$SmCl_3$·xLiCl and BM-$SmCl_3$·xLiCl (see Methods for details). As shown in **Figure S1 and S2**, the highest ionic conductivity was achieved with BM-$SmCl_3$·0.5LiCl. Interestingly, the BM-$SmCl_3$·0.5LiCl exhibited a Li-ion conductivity (1.2×10^{-4} S/cm) significantly higher than that of BM-LiCl (1×10^{-8} S cm^{-1}) and CM-$SmCl_3$·0.5LiCl (3.1×10^{-8} S cm^{-1}) at 30 °C (**Figure 2(d)**). The ionic transport in BM-$SmCl_3$·0.5LiCl was reflected by the dispersive regime (**Figure 2(e)**) at higher frequencies with a fitted n value of 1 according to the Jonscher's power law ($\sigma(\omega) = \sigma_{dc} + A\omega^n$), indicating that the ionic diffusion (hopping transition) is probably the dominant contributor to the conductivity.[28-30] The corresponding Nyquist plots and fitted curve at RT for the BM-$SmCl_3$·0.5LiCl are shown in **Figure S3**. The electronic conductivity of BM-$SmCl_3$·0.5LiCl was determined to be sufficiently low (2.49×10^{-9} S cm^{-1}) via chronoamperometry measurements (**Figure S4**). As presented in the XRD patterns of prepared materials (**Figure 2(f)**), both BM-$SmCl_3$·0.5LiCl and CM-$SmCl_3$·0.5LiCl presented a majority phase of $P6_3/m$, except that crystalline LiCl was detected in the CM-$SmCl_3$·0.5LiCl (marked as '*'). Since Li-ions are too small to stay in the Sm site, it is reasonable to observe a LiCl phase segregation after heat treatment. Unlike recently reported Li-M-Cl SSEs that generate a new crystal structure, both CM-$SmCl_3$·0.5LiCl and BM-$SmCl_3$·0.5LiCl preserve the framework structure ($P6_3/m$, UCl_3 type) of $SmCl_3$. Thus, the origin of the difference in ionic conductivity should be the presence or absence of mobile Li-ions along the frame channels.

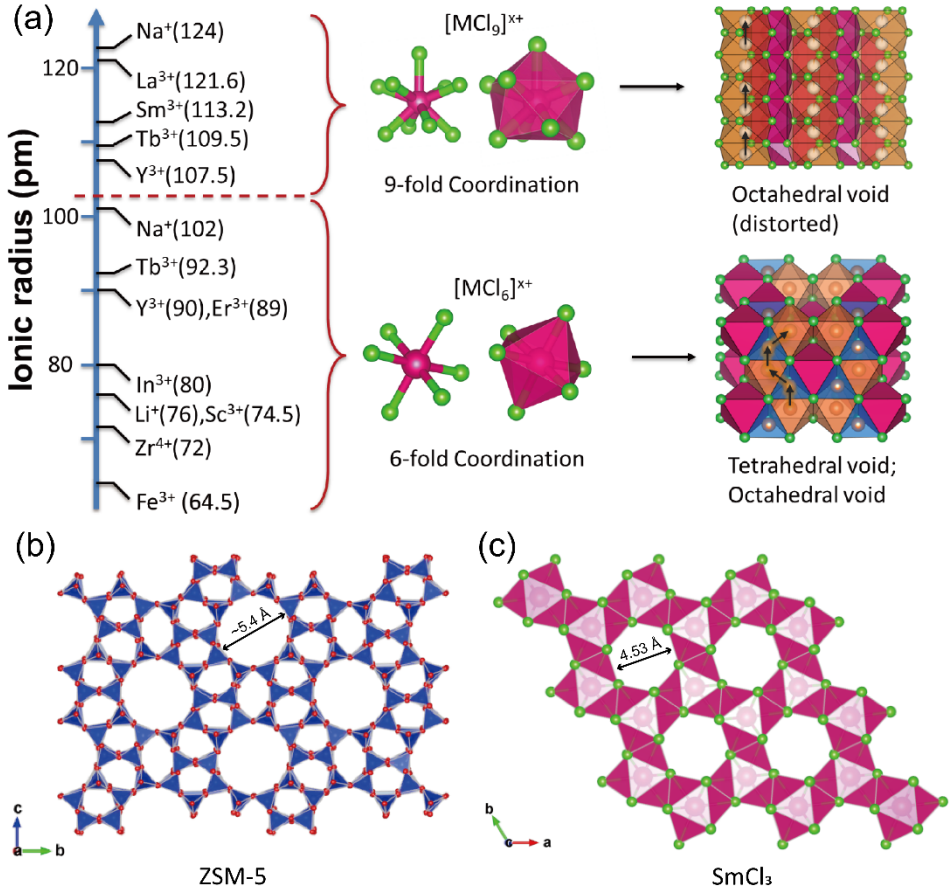

Figure 1 The porous framework structure based on halides. (a) The relationship between the ionic radius of M and the coordination of [MCl_x] polyhedra. The black arrows on the crystal structures indicate the Li-ion diffusion pathway. (b) The crystal lattice of a typical zeolite material, ZSM-5, with a pore size of ~5.4 Å. (c) Top view of $SmCl_3$ lattice along the *c*-axis to show the existing plentiful channels with an inner diameter of 4.53 Å.

To probe the structural relationship between LiCl and $SmCl_3$ in BM-$SmCl_3$·0.5LiCl, synchrotron-based XRD patterns of the BM-$SmCl_3$ and BM-$SmCl_3$·0.5LiCl were analyzed by Rietveld refinements (**Figure 3(a)**). If LiCl reacted with $SmCl_3$ to form a $Li_{2x}(Li_xSm_{2-x})Cl_6$ or a $Li_{3x}(Sm_{2-x}V_x)Cl_6$ crystalline phase, a crystal lattice shrinkage should be expected because Li^+ is much smaller than Sm^{3+}. However, no obvious difference in lattice parameters can be observed between BM-$SmCl_3$ and BM-$SmCl_3$·0.5LiCl. The accurate unit cell of the BM-$SmCl_3$ sample contained two crystallographic atom positions (Sm1, Cl1) was obtained by Rietveld refinement as shown in **Table S1**. The unit cell of BM-$SmCl_3$·0.5LiCl was almost identical to that of BM-$SmCl_3$ (**Table S2**), suggesting that Li^+ did not substitute the Sm^{3+} in the $SmCl_3$ framework. As another counterexample shown in **Figure S5**, $Na_{0.5}SmCl_{3.5}$ was synthesized through the same ball-milling process, and the XRD pattern presents a shift to the lower angle when compared with BM-$SmCl_3$ and BM-$SmCl_3$·0.5LiCl. A peak splitting at around $2\theta = 44$ ° was further observed due to the Na^+ substitution to Sm^{3+}, which was also absent for the BM-

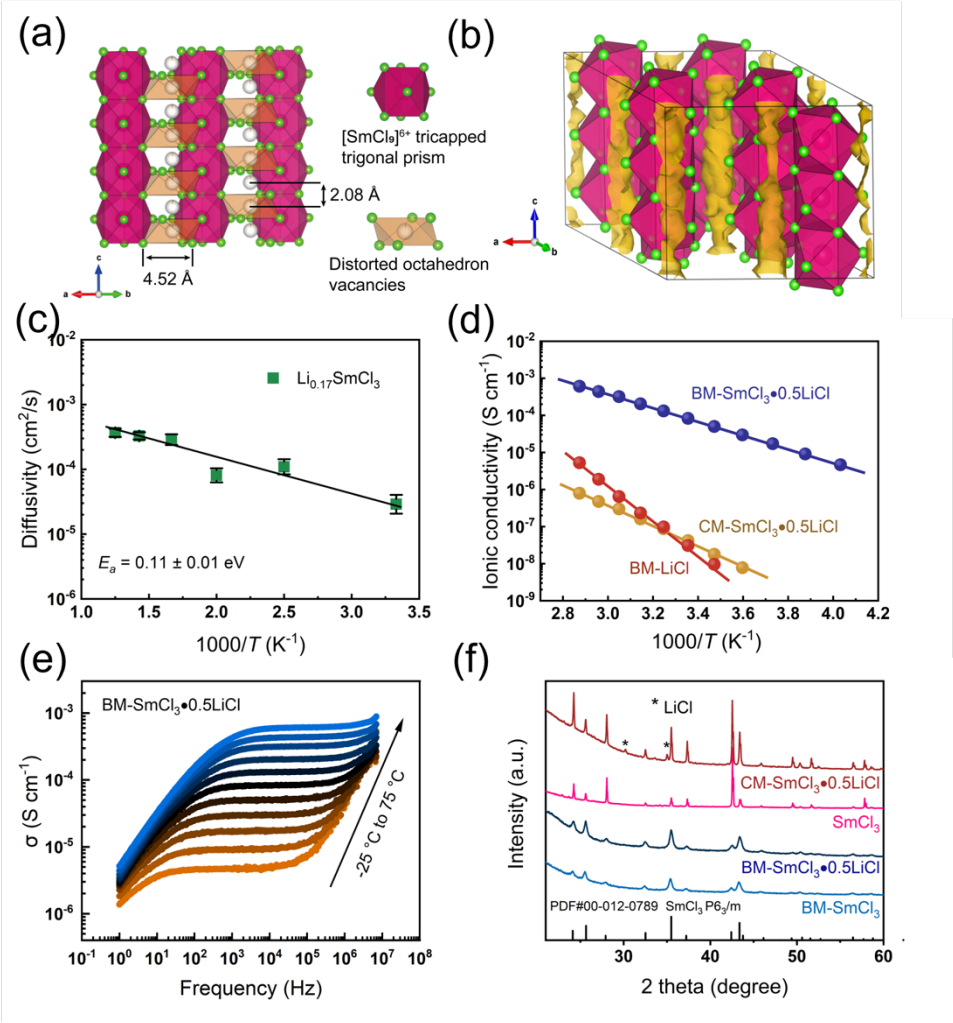

Figure 2 Theoretical calculations and experimental results of ionic diffusion in the $SmCl_3$ halide system. (a) The demonstration of Li-ion diffusion pathway in $SmCl_3$, with possible Li-ion sites indicated as white balls. (b) Crystal structure of $SmCl_3$ superimposed with Li-ion probability density (yellow iso-surface) from AIMD simulations of $Li_{0.17}SmCl_3$ at 300K. (c) The Arrhenius plot of Li-ion diffusivity from AIMD simulations of $Li_{0.17}SmCl_3$. (d) Arrhenius-plots of the BM-$SmCl_3$·0.5LiCl, CM-$SmCl_3$·0.5LiCl, and BM-LiCl. (e) Conductivity isotherms σ(ν) of the as-prepared BM-$SmCl_3$·0.5LiCl SSE recorded at different temperatures. (f) XRD patterns of BM-$SmCl_3$·0.5LiCl, CM-$SmCl_3$·0.5LiCl, $SmCl_3$, and BM-$SmCl_3$.

$SmCl_3$·0.5LiCl ($Li_{0.5}SmCl_{3.5}$), indicating the diffraction peaks of the BM-$SmCl_3$·0.5LiCl were derived from the intact $SmCl_3$ structure. The average crystallite sizes of BM-$SmCl_3$ and BM-$SmCl_3$·0.5LiCl samples were determined as 32.3 nm and 30.3 nm in diameter, respectively, according to the Scherrer equation[17, 31]. It is worth noting that the long-range ordering of LiCl was also absent in our observation of SPXRD, as the weight ratio of LiCl in BM-$SmCl_3$·0.5LiCl was below 0.001 according to the Rietveld refinement. It is hard to locate the lithium position and content through the diffraction method.

The total scattering technique coupled with Fourier transform and pair distribution function

(PDF) analysis stands out as an effective tool to probe the local structure and quantify the nanophase. **Figure 3(b)** and **Table S3** display the fits to the experimental PDFs, G(r), of BM-$SmCl_3$·0.5LiCl. Medium-range local structure analysis was carried out using the composite model: $SmCl_3$ (*P6₃/m*) + LiCl (*Fm-3m*) from 10 to 40 Å in real space. The BM-$SmCl_3$·0.5LiCl was fitted well with an Rw = 0.135 using the $SmCl_3$ and LiCl combination model. Quantitatively, the refinements of the G(r) revealed that the fitted weight ratios of $SmCl_3$ (0.923 ± 0.047) and LiCl (0.077 ± 0.047) are well consistent with the stoichiometric weight ratios of $SmCl_3$ (0.924) and LiCl (0.076) raw materials. Combining the synchrotron-based XRD refinements and PDF fitting suggests that the crystallinity of LiCl in the composite was interrupted under mechanical forces and the presence of $SmCl_3$ particles. Differential pair distribution function (d-PDF) analysis (**Figure 3(c)**) was conducted within a short range of 6 Å for BM-$SmCl_3$·0.5LiCl and BM-$SmCl_3$ to capture the possible interfacial bonding between $SmCl_3$ and LiCl. The most obvious difference is that BM-$SmCl_3$·0.5LiCl has a more intense peak at 2.85 Å than that of BM-$SmCl_3$, corresponding to the Sm-Cl distance. This can be originated from the bonding between Cl^- of LiCl and the surface coordinated unsaturated $SmCl_3$ nanocluster. The bonding characteristics of the Sm atoms in $[SmCl_{3+x}]^{x-}$ have been further confirmed by EXAFS analysis. The Fourier-transformed (FT) k^2-weighted $\chi(k)$ Sm L_3-edge EXAFS spectra of BM-$SmCl_3$ and BM-$SmCl_3$·0.5LiCl in **Figure 3(d)** demonstrate that the main peak located at R ≅ 2.3 Å without phase correction should be ascribed to the backscattering from Cl^- coordination. The BM-$SmCl_3$·0.5LiCl has a more intense peak than that of BM-$SmCl_3$ in R space, which is consistent with the d-PDF result. To quantify, we performed the EXAFS Sm-Cl bonding-specific curve-fitting analysis (**Figure S6 and Table S4**). The average Sm environment in $[SmCl_9]^{6+}$ comprises first-shell Sm-Cl with coordination number N = 8.3 ± 1.2 and distance R = 2.84 ± 0.01 Å for BM-$SmCl_3$, and N = 10.6 ± 1.3 and R = 2.85 ± 0.01 Å for BM-$SmCl_3$·0.5LiCl. The Sm-Cl distance derived from EXAFS analysis is in agreement with the distances derived from PDF (2.85 Å) and XRD (2.866 Å) results. Collectively, the increase of coordination number derived from experimental data agrees with the hypothesis that additional Cl^- filled the surface vacancies on $SmCl_3$, strongly suggesting that LiCl bonds to the $SmCl_3$ host rather than resulting from a solid-phase reaction between LiCl and $SmCl_3$. The composite of LiCl grafted onto the $SmCl_3$ grain was further confirmed by HR-STEM and SAED analyses in **Figure S7-S8**. $SmCl_3$ grains are widespread in the particle with random orientations and interconnected by the amorphous region or short-range crystalline region. According to the lattice fringes and spectroscopy analyses above, the connection region should be LiCl or amorphous $SmCl_3$ due to ball-milling treatment.

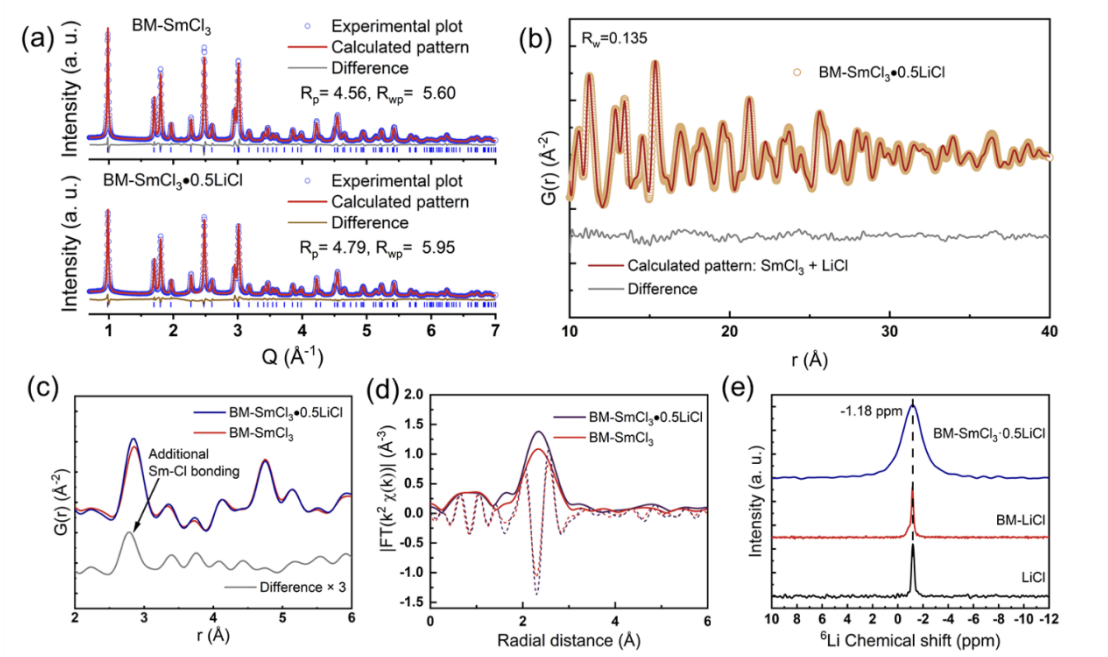

Figure 3 Structure determination of BM-$SmCl_3$·0.5LiCl. (a) The synchrotron-based XRD results and the Rietveld refinements: BM-$SmCl_3$ (top) and BM-$SmCl_3$·0.5LiCl (bottom). (b) The pair distributed function and fitting results of BM-$SmCl_3$·0.5LiCl. (c) The differential pair distribution function curve of BM-$SmCl_3$ and BM-$SmCl_3$·0.5LiCl with the difference between two curves as shown in the bottom. (d) Fourier transform of the Sm L_3-edge EXAFS in R-space, with a k^2-weighing. (e) ^{6}Li MAS NMR spectra of the BM-$SmCl_3$·0.5LiCl, BM-LiCl, and LiCl.

Both ^{6}Li and ^{7}Li magic-angle spinning (MAS) NMR spectroscopy can be used to investigate the local environment around Li-ions. Comparatively, ^{6}Li MAS spectra tend to give a better resolution as ^{6}Li nuclei experience comparatively weaker homonuclear dipole-dipole interactions due to their small magnetogyric ratio. For this reason, ^{6}Li MAS spectra of BM-$SmCl_3$·0.5LiCl and BM-LiCl along with pure solid LiCl were acquired and are shown in **Figure 3(e)**. The spectra of the BM-LiCl and the BM-$SmCl_3$·0.5LiCl samples display a strong peak at -1.18 ppm. The chemical shift values are the same as that of solid LiCl, confirming the occurrence of LiCl in BM-$SmCl_3$·0.5LiCl without the formation of Li-Sm-Cl or interference of the $SmCl_3$ framework. The broad signal with low intensity at -0.92 ppm in the BM-LiCl sample implies that some amorphous materials are formed by the mechanical treatment.[32-34] The peak in the spectrum of the BM-$SmCl_3$·0.5LiCl sample is rather broad, indicating a disordered local environment around the LiCl unit, which supports the conclusion derived from the synchrotron-based XRD refinement and the PDF fitting that the crystallinity of the LiCl in the composite has been diminished by mechanical forces.

Here, due to the structural similarity between $SmCl_3$ and zeolites, a host-adsorbent model is

proposed as shown in **Figure 4(a)**. The long-range crystallinity and chemical bond of LiCl was interrupted under mechanical forces so that nano-crystalline or amorphous LiCl was grafted to the $SmCl_3$ frame via ball-milling to provide mobile Li-ions hopping along the $SmCl_3$ channels. To confirm the adsorption-like mechanism on the surface and interface of $SmCl_3$ clusters, the surface-bulk heterogeneity in the LiCl-$SmCl_3$ composite and electron transfer between LiCl and $SmCl_3$ was revealed by a combined XPS and XAS study. The XPS spectra of Sm 3d and Cl 2p orbitals of BM-$SmCl_3$, BM-$SmCl_3$·0.5LiCl, and CM-$SmCl_3$·0.5LiCl were investigated to reveal the chemical and electronic states of the particle surface. In the Cl 2p spectra (**Figure 4(b)**), BM-$SmCl_3$ demonstrated two sets of doublets, depicted with blue peaks and red peaks. The red peaks refer to the subsurface Cl in $SmCl_3$, whereas the shifted blue peaks might be originated from the surface species due to the surface core-level shift.[35-36] After introducing LiCl through ball-milling, a new doublet (yellow peaks) arose and dominated at 199.2 eV and 200.9 eV in BM-$SmCl_3$·0.5LiCl, which can be assigned to the Li-Cl bonding (or Li-Cl-Sm),[37] suggesting the LiCl surface-enrichment. In CM-$SmCl_3$·0.5LiCl, the surface enrichment of LiCl was reduced, which is consistent with the LiCl-$SmCl_3$ phase separation observed in the previous XRD results. A peak shifting to the lower energy of Sm 3d spectra was observed in BM-$SmCl_3$·0.5LiCl compared to that of BM-$SmCl_3$ and CM-$SmCl_3$·0.5LiCl (**Figure S7**), which is due to the electron donation from the surface additional Cl^- to Sm^{3+}.

X-ray absorption near edge structure (XANES) can provide a comparison of surface and bulk electronic structure via switching the detection modes between total electron yield (TEY, < 10 nm depth) and fluorescence yield (FLY, ~50-100 nm depth), especially in the soft and tender X-ray region such as the Cl K-edge. Cl K-edge XANES of BM-$SmCl_3$·0.5LiCl, BM-$SmCl_3$, and BM-LiCl are studied via TEY and FLY modes, as shown in **Figure 4(c)** with solid lines as TEY-detected and dashed lines as FLY-detected. The pre-edge-feature a' was assigned to transitions from Cl 1s to the mixing state of Cl 3p and Sm 5d, and feature b' was assigned to transitions from Cl 1s to unoccupied Cl 4p-state.[38] The reference BM-$SmCl_3$ has a strong pre-edge signal due to the Sm-Cl hybridization, whereas BM-LiCl only presents a main transition feature b'. Both BM-$SmCl_3$ and BM-LiCl are looking similar in TEY mode and FLY mode except for the intensity shrinkage due to the self-absorption effect. As expected, BM-$SmCl_3$·0.5LiCl demonstrated different features in TEY mode and FLY mode. The rising edge b' of BM-$SmCl_3$·0.5LiCl is much stronger in TEY than in FLY, indicating a higher LiCl concentration on the surface. Quantitative analysis of the composite component of BM-$SmCl_3$·0.5LiCl was studied through linear combination fitting with BM-$SmCl_3$ and BM-LiCl, as shown in **Figure 4(d, e)**. From surface to bulk, the LiCl contribution was reduced from 36 %

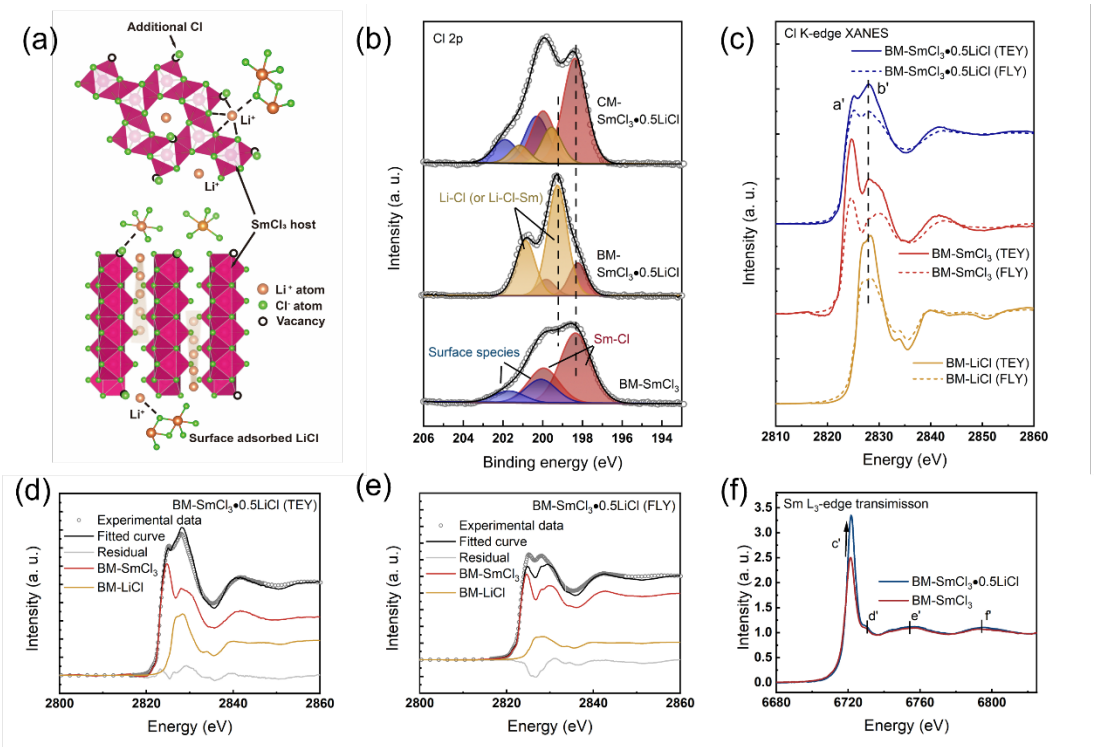

Figure 4 The surface-bulk heterogeneity in BM-$SmCl_3$·0.5LiCl. (a) Schematic host-adsorbent model of LiCl adsorbing onto $SmCl_3$ clusters. (b) Cl 2p XPS spectra of BM-$SmCl_3$, BM-$SmCl_3$·0.5LiCl, and CM-$SmCl_3$·0.5LiCl. (c) The XANES region of Cl K-edge of BM-$SmCl_3$·0.5LiCl, BM-$SmCl_3$, and BM-LiCl in TEY and FLY detect mode. (d-e) Linear combination fitting of BM-$SmCl_3$·0.5LiCl in TEY (d) and FLY (e). (f) The XANES region of Sm L_3-edge of BM-$SmCl_3$·0.5LiCl and BM-$SmCl_3$ in transmission mode.

to 20 % (theoretically, it should be ~15 % for a uniform distribution), confirming that LiCl covered the $SmCl_3$ surface to form a core-shell-like structure. In the Sm L_3-edge XANES of transmission detected mode, four different characteristic peaks are marked as c', d', e', and f'. The rising edge feature c' and feature d' originated from electric-dipole allowing transitions from Sm 2p-orbitals to unoccupied states that contain Sm 5d character ($2p^6\ 4f^6\ 5d^0 \rightarrow 2p^5\ 4f^6\ 5d^1$ transitions). Features e' and f' can be assigned to the multiple scattering resonance or the transition to quasi-bound states.[39] Interestingly, relative to the BM-$SmCl_3$, the BM-$SmCl_3$·0.5LiCl has a noticeable sharper white line a' just above the threshold (**Figure 4(f)**). The Sm L_3-edge XANES in transmission reveals an increase in the density of unoccupied 5d states (a bulk effect), i.e., loss of electrons, which is contrary to surface Sm 3d XPS results (gain of electrons) for BM-$SmCl_3$·0.5LiCl. This contradiction can be explained by the surface-bulk heterogeneity due to the LiCl bonding to the surface of $SmCl_3$ nanoparticles, generating an $[SmCl_{3+x}]^{x-}$ negative-charged framework and surface Li^+ ions. The combination of XPS and XAS has confirmed a core-shell-like structure of BM-$SmCl_3$·0.5LiCl, supporting the host-

adsorbent model.

The morphology of $SmCl_3$, BM-$SmCl_3$, BM-$SmCl_3$·0.5LiCl, and CM-$SmCl_3$·0.5LiCl are present in **Figure S9**. The ball-milling process significantly reduces the particle size of $SmCl_3$ from the micron-scale (pristine $SmCl_3$) to the nanoscale (BM-$SmCl_3$). Interestingly, the BM-$SmCl_3$·0.5LiCl presents different morphological characteristics, which have a smooth surface and are well-connected between different particles. LiCl appears to "coat" onto the $SmCl_3$ particles to help build a well-connected network. As for the co-melting method, large particles with fractures were generated again in CM-$SmCl_3$·0.5LiCl. We believed that the LiCl is separated from $SmCl_3$ according to the XRD results. In the Raman spectra of **Figure S10**, a strong fluorescent signal was presented in the ball-milling samples, whereas it was absent in pristine $SmCl_3$ and CM-$SmCl_3$·0.5LiCl. One possible reason is that the ball-milling process creates abundant surface defects on $SmCl_3$ nanoparticles, giving rise to a strong fluorescent signal. We presume that the surface defects of $SmCl_3$ provide anchoring sites for LiCl.

The relationship between ionic diffusion behaviors and the host-adsorbent state was further studied. The differential scanning calorimetry (DSC) results of BM-$SmCl_3$·0.5LiCl are shown in **Figure 5(a)**. A sharp endothermal peak at 445 °C refers to the melting process of BM-$SmCl_3$·0.5LiCl. Before the melting point, there are one exothermal peak and two endothermal peaks at around 150°C, 300 °C, and 360 °C, respectively, suggesting that several metastable phases existed. **Figure 5(b)** shows the ionic conductivity after annealing the BM-$SmCl_3$·0.5LiCl at different temperatures for 10 hours. The ionic conductivity of the annealed sample significantly decreased once the annealing temperature was higher than 150 °C, corresponding to the first exothermal peak. The decrease of rising edge feature c' of Sm L_3-edge of BM-$SmCl_3$·0.5LiCl@150°C in **Figure 5(c)** indicates the possible destruction of the bound state between $SmCl_3$ and LiCl. *In-situ* temperature-dependent XRD (**Figure 5(d)**) was studied to determine the presence of metastable phases. As the temperature increased, three metastable crystal phases were detected in a sequence, namely α-Li-Sm-Cl, β-Li-Sm-Cl, and γ-Li-Sm-Cl, matching well with DSC results. It is hard to identify the three metastable crystal phases since no Li-Sm-Cl structures have been reported so far. However, the results still revealed that the fast ionic diffusion is directly related to the bound state of LiCl. Once the bound state was damaged along with the formation of crystalline Li-Sm-Cl, the loss of movable lithium ions in the channel give rise to the decrease of ionic conductivity.

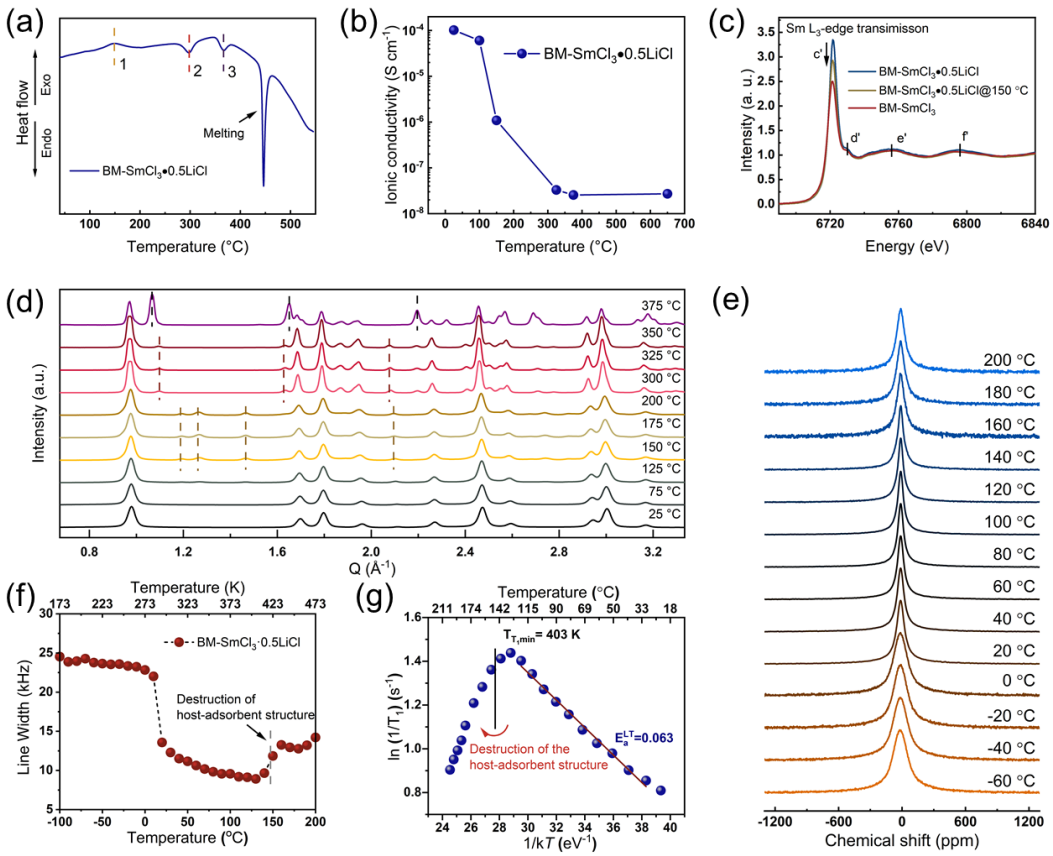

Figure 5 Temperature-dependent ionic diffusion behaviors in BM-$SmCl_3$·0.5LiCl. (a) The DSC curve of the BM-$SmCl_3$·0.5LiCl. (b) Ionic conductivities of BM-$SmCl_3$·0.5LiCl annealed at different temperatures for 10 h. (c) The XANES region of Sm L_3-edge of BM-$SmCl_3$, BM-$SmCl_3$·0.5LiCl, and BM-$SmCl_3$·0.5LiCl@150 °C (annealed at 150 °C for 10 h) in transmission mode. (d) *In-situ* XRD results of BM-$SmCl_3$·0.5LiCl at elevated temperatures. (e) Temperature dependence of the ^{7}Li NMR spectra of BM-$SmCl_3$·0.5LiCl observed at various temperatures ranging from -60 °C to 200 °C. (f) Motional narrowing of the line width of the ^{7}Li NMR central transition of BM-$SmCl_3$·0.5LiCl sample. The rigid-lattice regime is reached at a temperature lower than 283 K (10 °C). (g) Temperature dependence of diffusion-induced ^{7}Li NMR SLR rates in the laboratory frame of reference for BM-$SmCl_3$·0.5LiCl. The Larmor frequency is 155.2 MHz.

The evolution of Li-ion dynamics is further examined by motional narrowing (MN) studies of the ^{7}Li static NMR spectra of BM-$SmCl_3$·0.5LiCl. **Figures 5(e-f)** show that the static ^{7}Li NMR spectra were obtained in a temperature range from -100 to 200 °C. The changes in the linewidth as a function of temperature were identified in three regions qualitatively in **Figure 5(e)** visually and quantitatively in **Figure 5(f)**. At lower temperatures (below 0 °C), the full width at half maximum (FWHM) was large and dominated by the dipolar coupling of the nuclear spins of ^{7}Li achieving the rigid-lattice regime. At 0 °C, a sudden decrease in FWHM was observed. The abrupt change in FWHM at 0 °C was due to the fact that the Li-Li dipolar interactions were drastically averaged by thermally activated motions of Li ions, i.e., the rapid Li-ion diffusions.

Between 0 °C and 140 °C, the FWHM gradually decreased with increasing temperature. Interestingly, when the temperature was above 140 °C, an increase in FWHM with increasing temperature was observed. The FWHM within the temperature between 160-200 °C was around 14 kHz. This abnormal thermal behavior is consistent with the in-situ XRD result that the material undergoes a phase transition to a metastable phase with lower Li-ion diffusion rates at elevated temperatures above 150 °C.

The temperature-dependent ^{7}Li static spin-lattice relaxation (SLR) rates in the laboratory frame of reference ($1/T_1$) were measured to determine activation energies of lithium-ion diffusions as the $1/T_1$ is directly related to the spectral density function of the Li-ion jumping process.[40-41] As shown in **Figure 5(g)**, below the phase transition temperature (150 °C), a $1/T_1$ maximum was reached at 130 °C, and the ln ($1/T_1$) versus temperature (T) plot satisfied an Arrhenius behavior in the low-temperature regime. The activation energy of the low-temperature flank (E_a^{LT}) was determined as low as 0.063 eV for the BM-$SmCl_3$·0.5LiCl sample, corresponding to the short-range Li-ion diffusion, which is in agreement with the estimated energy barrier in AIMD simulations (**Figure 2(c)**). In the laboratory frame of reference, an absolute lithium jump rate can be deduced from the maximum condition ($\tau \cdot \omega_o \approx 1$) at the relaxation rate peak where the τ represents the average correlation time/residence time between subsequent hops.[42-45] Considering this condition, the Larmor frequency of $\omega_0/(2\pi)$ = 155.2 MHz results in a Li-ion jump frequency/jump rate (τ^{-1}) of 9.8×10^8 s^{-1} at 403 K. It is reported that the residence time τ in the ns regime corresponds to an ionic conductivity on the order of 10^{-3} S cm^{-1},[43, 46] implying a reasonable conductivity at 130 °C.

The above-shown data clearly show that the bound state between $SmCl_3$ crystalline and grafted LiCl is responsible for the fast ionic diffusion. However, even for BM-$SmCl_3$·0.5LiCl, the ionic conductivity is still two to three orders of magnitude below the theoretically calculated value of the framework. We consider that there should be other factors influencing ion transport. For example, diffusion within 1D channels severely depends on lattice continuity. The fast ion diffusion according to the theoretical calculation would be compromised due to lattice mismatch in practical cases. Thus, the grafted LiCl between different $SmCl_3$ domains is not only a provider of mobile Li-ion but also an important connection of mismatched $SmCl_3$ clusters. The poor diffusion properties of LiCl reduce inter-grain diffusion and make it a rate-limiting step. In this regard, the ionic conductivity should be related to the domain size of $SmCl_3$. The ionic conductivities upon different BM conditions (**Figure S2**) and corresponding nano-structural analyses (**Figure S15**) demonstrated that the domain size of the $SmCl_3$ critically affects the ionic conductivity, consistence with the assumption.

We also replaced $SmCl_3$ in BM-MCl_3·0.5LiCl with MCl_3 (M = La, Ce, Pr, Nd) to demonstrate

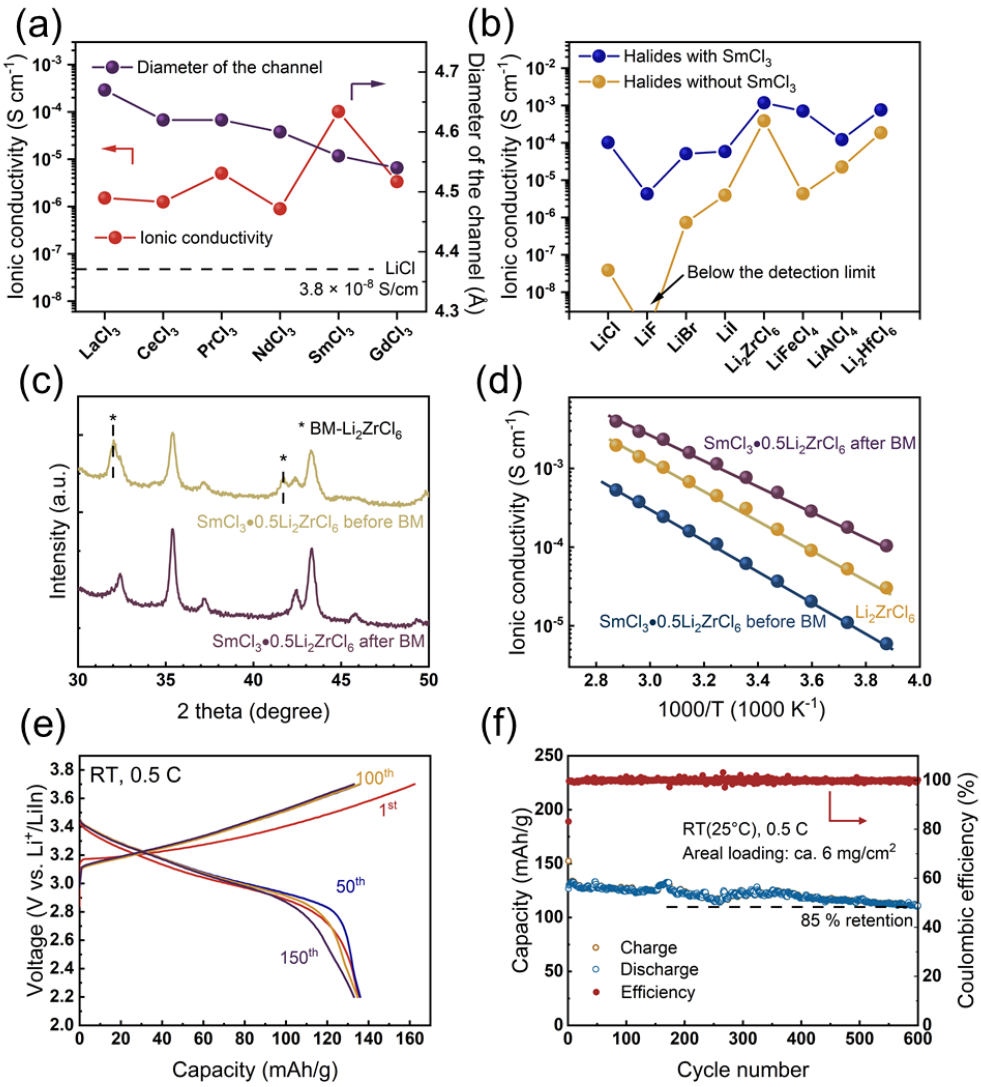

Figure 6 Demonstration of the universality of ionic diffusion behavior in the $SmCl_3$ framework and battery performance. (a) The ionic conductivities of different frameworks MCl_3 (M = La, Ce, Pr, Nd) coupled with 0.5 LiCl (molar ratio) at 30°C. (b) The ionic conductivities of $SmCl_3$ framework coupled with different halide adsorbents at 30°C. (c) XRD patterns of the $SmCl_3{\cdot}0.5Li_2ZrCl_6$ before and after ball-milling. (d) Arrhenius-plots of Li_2ZrCl_6 and the $SmCl_3{\cdot}0.5Li_2ZrCl_6$ (before and after ball-milling). (e) The charge and discharge voltage profiles of the ASSLIB using $LiNi_{0.83}Mn_{0.06}Co_{0.11}O$ (NMC83) as cathode and $SmCl_3{\cdot}0.5Li_2ZrCl_6$ as SSE layer at different cycles (1^{st}, 50^{th}, 100^{th}, and 150^{th}). (f) Plots of capacity and Coulombic efficiency versus cycling numbers of the ASSLIB in (e).

the universality of ionic diffusion behaviors in the host-adsorbent structure. All of them presented faster Li-ion diffusion than that of pure LiCl, as shown in **Figure 6(a)**. A slight increase in ionic conductivity can be observed along with the decrease in the diameter, but the $NdCl_3$ and $GdCl_3$ cases do not follow the trend. We further replace the LiCl in BM-$SmCl_3{\cdot}0.5LiCl$ with LiF, LiBr, LiI, or even Li-M-Cl, such as $LiFeCl_4$, Li_2ZrCl_6, and $LiAlCl_4$ (**Figure 6(b)**). The comparison between samples with and without $SmCl_3$ confirmed the boosting effect of $SmCl_3$ on the ionic conductivity of the composites. The corresponding

diffraction signal of adsorbents disappeared in the composite after ball-milling treatment (**Figures S18 and S19**). Taking the $SmCl_3 \cdot 0.5Li_2ZrCl_6$ as an example, the diffraction peaks of BM-Li_2ZrCl_6 disappeared after ball-milling with $SmCl_3$ (**Figure 6(c)**), indicating the interruption of its crystallinity due to the coating form onto the $SmCl_3$ nanoparticles. After ball-milling, its ionic conductivity increased by ~10 times compared to that before ball-milling, even higher than the pure Li_2ZrCl_6 SSE (**Figure 6(d)**). The application potential of the $SmCl_3$ framework-based SSEs was demonstrated by constructing ASSLIBs using BM-$SmCl_3 \cdot 0.5Li_2ZrCl_6$ as the SSE layer. $LiNi_{0.83}Mn_{0.06}Co_{0.11}O_2$ (NMC83) was selected as a cathode active material for ASSLIBs evaluations, and detailed cell configurations were described in the Methods. The ASSLIB with BM-$SmCl_3 \cdot 0.5Li_2ZrCl_6$ as the SSE layer exhibited excellent cycle performance under 0.5 C (1 C = 200 mAh g^{-1}) in a voltage range of 2.2 - 3.7 V (vs. Li^+/LiIn). The charge-discharge curves in **Figure 6(e)** depicted a high reversible charge-discharge process and lower voltage decay at the 1st, 50th, 100th, and 150th cycles, respectively. As shown in **Figure 6(f)**, the ASSLIB with BM-$SmCl_3 \cdot 0.5Li_2ZrCl_6$ SSE demonstrated highly stable cycling performance for over 600 cycles with a capacity retention of 85%.

Conclusion

In summary, we reported a new class of zeolite-like halide frameworks, $SmCl_3$ for example, in which 1-dimensional channels were enclosed by $[SmCl_9]^{6-}$ tricapped trigonal prisms, providing a short jumping distance of 2.08 Å between vacancies for Li-ion hopping. The fast Li-ion diffusion along the channels was verified through AIMD calculations and *in-situ* NMR measurements. Combining the structure and bonding analysis, we propose a zeolite-like host-adsorbent structure prepared by a ball-milling process, generating delocalized Li-ion moving through the 1D channels in the $SmCl_3$ framework. The ionic conductivity of the BM-$SmCl_3 \cdot 0.5LiCl$ and BM-$SmCl_3 \cdot 0.5Li_2ZrCl_6$ SSEs are over 10^{-4} S cm^{-1} and 10^{-3} S cm^{-1} at 30 °C, respectively. Moreover, the interfacial bonding behavior and ionic diffusion of the class of frameworks were demonstrated to be universal across different halides, presenting ionic conductivities ranging from 10^{-6}-10^{-3} S/cm. It is suggested that the ionic conductivity of the $LnCl_3$/halide composite (Ln = La-Gd) is likely in correlation with the ionic conductivity of halide, interfacial bonding, and framework composition/dimensions. This work reveals a potential class of structures in halides for fast superionic conductors, which will broaden the horizon of superionic conductor design and contribute to a wider selection of halide SSEs.

Acknowledgments

This research was supported by the Natural Sciences and Engineering Research Council of Canada (NSERC), Canada Research Chair Program (CRC), Canada Foundation for Innovation (CFI), Ontario Research Fund, the Canada Light Source at the University of Saskatchewan (CLS), Interdisciplinary Development Initiatives (IDI) by Western University, Canada MITACS fellow, and University of Western Ontario. The authors also appreciate the help of the beamline scientist of HXMA (Dr. Weifeng Chen), VESPERS (Dr. Renfei Feng), and SXRMB (Dr. Mohsen Shakouri, Dr. Qunfeng Xiao, and Dr. Alisa Paterson) beamline at Canadian Light Source, 20-BM/ID (Dr. Zou Finfrock, Dr. Debora Motta Meira, and Dr. Michael Pape) at Advanced Photon Source, and 19A (Dr. Yu-Chun Chuang) at Taiwan Photon Source. Y. M. acknowledges the funding support from the US National Science Foundation Award# 1940166 and the computational facilities from the University of Maryland supercomputing resources and the Maryland Advanced Research Computing Center (MARCC).

Reference:

1. Harper, G.; Sommerville, R.; Kendrick, E.; Driscoll, L.; Slater, P.; Stolkin, R.; Walton, A.; Christensen, P.; Heidrich, O.; Lambert, S.; Abbott, A.; Ryder, K.; Gaines, L.; Anderson, P., Recycling lithium-ion batteries from electric vehicles. *Nature* **2019,** *575* (7781), 75-86.
2. Sun, Y.-K., Promising All-Solid-State Batteries for Future Electric Vehicles. *ACS Energy Letters* **2020,** *5* (10), 3221-3223.
3. Albertus, P.; Anandan, V.; Ban, C.; Balsara, N.; Belharouak, I.; Buettner-Garrett, J.; Chen, Z.; Daniel, C.; Doeff, M.; Dudney, N. J.; Dunn, B.; Harris, S. J.; Herle, S.; Herbert, E.; Kalnaus, S.; Libera, J. A.; Lu, D.; Martin, S.; McCloskey, B. D.; McDowell, M. T.; Meng, Y. S.; Nanda, J.; Sakamoto, J.; Self, E. C.; Tepavcevic, S.; Wachsman, E.; Wang, C.; Westover, A. S.; Xiao, J.; Yersak, T., Challenges for and Pathways toward Li-Metal-Based All-Solid-State Batteries. *ACS Energy Letters* **2021**, 1399-1404.
4. Asano, T.; Sakai, A.; Ouchi, S.; Sakaida, M.; Miyazaki, A.; Hasegawa, S., Solid Halide Electrolytes with High Lithium-Ion Conductivity for Application in 4 V Class Bulk-Type All-Solid-State Batteries. *Adv Mater* **2018,** *30* (44), e1803075.
5. Li, X.; Liang, J.; Chen, N.; Luo, J.; Adair, K. R.; Wang, C.; Banis, M. N.; Sham, T. K.; Zhang, L.; Zhao, S.; Lu, S.; Huang, H.; Li, R.; Sun, X., Water-Mediated Synthesis of a Superionic Halide Solid Electrolyte. *Angew Chem Int Ed Engl* **2019,** *58* (46), 16427-16432.
6. Zhou, L.; Kwok, C. Y.; Shyamsunder, A.; Zhang, Q.; Wu, X.; Nazar, L. F., A new halospinel superionic conductor for high-voltage all solid state lithium batteries. *Energy & Environmental Science* **2020,** *13* (7), 2056-2063.
7. Jung, S.-K.; Gwon, H.; Yoon, G.; Miara, L. J.; Lacivita, V.; Kim, J.-S., Pliable Lithium Superionic Conductor for All-Solid-State Batteries. *ACS Energy Letters* **2021,** *6* (5), 2006-2015.
8. Park, K.-H.; Kaup, K.; Assoud, A.; Zhang, Q.; Wu, X.; Nazar, L. F., High-Voltage

Superionic Halide Solid Electrolytes for All-Solid-State Li-Ion Batteries. *ACS Energy Letters* **2020,** *5* (2), 533-539.
9. Li, X.; Liang, J.; Luo, J.; Norouzi Banis, M.; Wang, C.; Li, W.; Deng, S.; Yu, C.; Zhao, F.; Hu, Y.; Sham, T.-K.; Zhang, L.; Zhao, S.; Lu, S.; Huang, H.; Li, R.; Adair, K. R.; Sun, X., Air-stable Li3InCl6 electrolyte with high voltage compatibility for all-solid-state batteries. *Energy & Environmental Science* **2019,** *12* (9), 2665-2671.
10. Liang, J.; Li, X.; Wang, S.; Adair, K. R.; Li, W.; Zhao, Y.; Wang, C.; Hu, Y.; Zhang, L.; Zhao, S.; Lu, S.; Huang, H.; Li, R.; Mo, Y.; Sun, X., Site-Occupation-Tuned Superionic LixScCl3+xHalide Solid Electrolytes for All-Solid-State Batteries. *J Am Chem Soc* **2020,** *142* (15), 7012-7022.
11. Wang, C.; Liang, J.; Luo, J.; Liu, J.; Li, X.; Zhao, F.; Li, R.; Huang, H.; Zhao, S.; Zhang, L.; Wang, J.; Sun, X., A universal wet-chemistry synthesis of solid-state halide electrolytes for all-solid-state lithium-metal batteries. *Science Advances* **2021,** *7* (37), eabh1896.
12. Wang, K.; Ren, Q.; Gu, Z.; Duan, C.; Wang, J.; Zhu, F.; Fu, Y.; Hao, J.; Zhu, J.; He, L.; Wang, C. W.; Lu, Y.; Ma, J.; Ma, C., A cost-effective and humidity-tolerant chloride solid electrolyte for lithium batteries. *Nat Commun* **2021,** *12* (1), 4410.
13. Kwak, H.; Han, D.; Lyoo, J.; Park, J.; Jung, S. H.; Han, Y.; Kwon, G.; Kim, H.; Hong, S. T.; Nam, K. W.; Jung, Y. S., New Cost-Effective Halide Solid Electrolytes for All-Solid-State Batteries: Mechanochemically Prepared Fe^{3+} - Substituted Li_2ZrCl_6. *Advanced Energy Materials* **2021**.
14. Schlem, R.; Muy, S.; Prinz, N.; Banik, A.; Shao-Horn, Y.; Zobel, M.; Zeier, W. G., Mechanochemical Synthesis: A Tool to Tune Cation Site Disorder and Ionic Transport Properties of Li_3MCl_6 (M = Y, Er) Superionic Conductors. *Advanced Energy Materials* **2019**.
15. Zhou, L.; Zuo, T.-T.; Kwok, C. Y.; Kim, S. Y.; Assoud, A.; Zhang, Q.; Janek, J.; Nazar, L. F., High areal capacity, long cycle life 4 V ceramic all-solid-state Li-ion batteries enabled by chloride solid electrolytes. *Nature Energy* **2022,** *7* (1), 83-93.
16. Helm, B.; Schlem, R.; Wankmiller, B.; Banik, A.; Gautam, A.; Ruhl, J.; Li, C.; Hansen, M. R.; Zeier, W. G., Exploring Aliovalent Substitutions in the Lithium Halide Superionic Conductor Li3–xIn1–xZrxCl6 ($0 \leqslant x \leqslant 0.5$). *Chemistry of Materials* **2021,** *33* (12), 4773-4782.
17. Shannon, R., Revised effective ionic radii and systematic studies of interatomic distances in halides and chalcogenides. *Acta Crystallographica Section A* **1976,** *32* (5), 751-767.
18. Wang, S.; Bai, Q.; Nolan, A. M.; Liu, Y.; Gong, S.; Sun, Q.; Mo, Y., Lithium Chlorides and Bromides as Promising Solid-State Chemistries for Fast Ion Conductors with Good Electrochemical Stability. *Angew Chem Int Ed Engl* **2019,** *58* (24), 8039-8043.
19. Liu, Y.; Wang, S.; Nolan, A. M.; Ling, C.; Mo, Y., Tailoring the Cation Lattice for Chloride Lithium-Ion Conductors. *Advanced Energy Materials* **2020**.
20. Sebti, E.; Evans, H. A.; Chen, H.; Richardson, P. M.; White, K. M.; Giovine, R.; Koirala, K. P.; Xu, Y.; Gonzalez-Correa, E.; Wang, C.; Brown, C. M.; Cheetham, A. K.; Canepa, P.; Clement, R. J., Stacking Faults Assist Lithium-Ion Conduction in a Halide-Based Superionic Conductor. *J Am Chem Soc* **2022**.
21. Jordan, E.; Bell, R. G.; Wilmer, D.; Koller, H. J. J. o. t. A. C. S., Anion-promoted cation motion and conduction in zeolites. **2006,** *128* (2), 558-567.
22. Zhao, R.; Wu, Y.; Liang, Z.; Gao, L.; Xia, W.; Zhao, Y.; Zou, R., Metal–organic frameworks for solid-state electrolytes. *Energy & Environmental Science* **2020,** *13* (8),

2386-2403.
23. Xu, W.; Pei, X.; Diercks, C. S.; Lyu, H.; Ji, Z.; Yaghi, O. M., A Metal-Organic Framework of Organic Vertices and Polyoxometalate Linkers as a Solid-State Electrolyte. *J Am Chem Soc* **2019,** *141* (44), 17522-17526.
24. Park, S. S.; Tulchinsky, Y.; Dinca, M., Single-Ion Li(+), Na(+), and Mg(2+) Solid Electrolytes Supported by a Mesoporous Anionic Cu-Azolate Metal-Organic Framework. *J Am Chem Soc* **2017,** *139* (38), 13260-13263.
25. Chi, X.; Li, M.; Di, J.; Bai, P.; Song, L.; Wang, X.; Li, F.; Liang, S.; Xu, J.; Yu, J., A highly stable and flexible zeolite electrolyte solid-state Li-air battery. *Nature* **2021,** *592* (7855), 551-557.
26. Lissner, F.; Krämer, K.; Schleid, T.; Meyer, G.; Hu, Z.; Kaindl, G. J. Z. f. a. u. a. C., Die Chloride Na3xM2–xCl6 (M= La Sm) und NaM2Cl6 (M= Nd, Sm): Derivate des UCl3-Typs. Synthese, Kristallstruktur und Röntgenabsorptionsspektroskopie (XANES). **1994,** *620* (3), 444-450.
27. Wickleder, M. S.; Meyer, G. J. Z. f. a. u. a. C., Neue Derivate des UCl3-Typs: Die Chloride und Bromide A (SrSm) Cl6, A (SrEu) Cl6 und A (BaLa) X6 (A= Na, Ag; X= Cl, Br). **1998,** *624* (10), 1577-1582.
28. Lee, W. K.; Liu, J. F.; Nowick, A. S., Limiting behavior of ac conductivity in ionically conducting crystals and glasses: A new universality. *Phys Rev Lett* **1991,** *67* (12), 1559-1561.
29. Dhahri, A.; Dhahri, E.; Hlil, E. K., Electrical conductivity and dielectric behaviour of nanocrystalline La0.6Gd0.1Sr0.3Mn0.75Si0.25O3. *RSC Advances* **2018,** *8* (17), 9103-9111.
30. Mauritz, K. A. J. M., Dielectric relaxation studies of ion motions in electrolyte-containing perfluorosulfonate ionomers. 4. Long-range ion transport. **1989,** *22* (12), 4483-4488.
31. Holzwarth, U.; Gibson, N., The Scherrer equation versus the 'Debye-Scherrer equation'. *Nat Nanotechnol* **2011,** *6* (9), 534.
32. Tatsumisago, M.; Yamashita, H.; Hayashi, A.; Morimoto, H.; Minami, T. J. J. o. n.-c. s., Preparation and structure of amorphous solid electrolytes based on lithium sulfide. **2000,** *274* (1-3), 30-38.
33. Nakagawa, Y.; Kimura, T.; Ohki, T.; Isobe, S.; Shibayama, T. J. S. S. I., Effect of mechanical milling on lithium-ion conductivity of LiAlH4. **2021,** *365*, 115656.
34. Rao, R. P.; Sharma, N.; Peterson, V.; Adams, S. J. S. S. I., Formation and conductivity studies of lithium argyrodite solid electrolytes using in-situ neutron diffraction. **2013,** *230*, 72-76.
35. Andersen, J. N.; Hennig, D.; Lundgren, E.; Methfessel, M.; Nyholm, R.; Scheffler, M., Surface core-level shifts of some 4d-metal single-crystal surfaces: Experiments and ab initio calculations. *Physical Review B* **1994,** *50* (23), 17525-17533.
36. Wertheim, G.; Buchanan, D.; Rowe, J.; Citrin, P., Surface-ion core-level shifts in alkali halides. *Surface science* **1994,** *319* (3), L41-L46.
37. Wren, A. G.; Phillips, R. W.; Tolentino, L. U. J. J. o. C.; Science, I., Surface reactions of chlorine molecules and atoms with water and sulfuric acid at low temperatures. **1979,** *70* (3), 544-557.
38. Shadle, S. E., *Ligand K-edge x-ray absorption spectroscopic studies of the electronic structure of inorganic model complexes and metalloprotein active sites*. Stanford University: 1994.

39. Soldatov, A.; Ivanchenko, T.; Della Longa, S.; Kotani, A.; Iwamoto, Y.; Bianconi, A. J. P. R. B., Crystal-structure effects in the Ce L 3-edge x-ray-absorption spectrum of CeO 2: Multiple-scattering resonances and many-body final states. **1994,** *50* (8), 5074.
40. Mehrer, H., *Diffusion in solids: fundamentals, methods, materials, diffusion-controlled processes*. Springer Science & Business Media: 2007; Vol. 155.
41. Springer, T.; Lechner, R., Diffusion in condensed matter. Springer New York: 2005.
42. Yu, C.; Ganapathy, S.; Hageman, J.; Van Eijck, L.; Van Eck, E. R.; Zhang, L.; Schwietert, T.; Basak, S.; Kelder, E. M.; Wagemaker, M. J. A. a. m.; interfaces, Facile synthesis toward the optimal structure-conductivity characteristics of the argyrodite Li6PS5Cl solid-state electrolyte. **2018,** *10* (39), 33296-33306.
43. Uitz, M.; Epp, V.; Bottke, P.; Wilkening, M. J. J. o. E., Ion dynamics in solid electrolytes for lithium batteries. **2017,** *38* (2), 142-156.
44. Wilkening, M.; Heitjans, P. J. C., From Micro to Macro: Access to Long-Range Li+ Diffusion Parameters in Solids via Microscopic 6, 7Li Spin - Alignment Echo NMR Spectroscopy. **2012,** *13* (1), 53-65.
45. Yu, C.; Ganapathy, S.; van Eck, E. R.; van Eijck, L.; Basak, S.; Liu, Y.; Zhang, L.; Zandbergen, H. W.; Wagemaker, M. J. J. o. M. C. A., Revealing the relation between the structure, Li-ion conductivity and solid-state battery performance of the argyrodite Li 6 PS 5 Br solid electrolyte. **2017,** *5* (40), 21178-21188.
46. Duchêne, L.; Lunghammer, S.; Burankova, T.; Liao, W.-C.; Embs, J. P.; Copéret, C.; Wilkening, H. M. R.; Remhof, A.; Hagemann, H.; Battaglia, C. J. C. o. M., Ionic conduction mechanism in the Na2 (B12H12) 0.5 (B10H10) 0.5 closo-borate solid-state electrolyte: interplay of disorder and ion–ion interactions. **2019,** *31* (9), 3449-3460.